J. Synchrotron Rad. (1998). **5**, 90–101

A Triple-Crystal Diffractometer for High-Energy Synchrotron Radiation at the HASYLAB High-Field Wiggler Beamline BW5

R. Bouchard, D. Hupfeld, T. Lippmann, J. Neuefeind, H.-B. Neumann, H. F. Poulsen,† U. Rütt, T. Schmidt, J. R. Schneider,* J. Süssenbach and M. von Zimmermann

Hamburger Synchrotronstrahlungslabor HASYLAB at Deutsches Elektronen-Synchrotron DESY, Notkestrasse 85, D-22603 Hamburg, Germany. E-mail: schneider@desy.de

(*Received 30 July 1997; accepted 24 October 1997*)

The triple-crystal diffractometer installed at HASYLAB beamline BW5 with a high-field wiggler of critical energy 27 keV for DORIS III, operated at 4.5 GeV electron energy, is described. Samples can be mounted in large cryostats or furnaces normally used in neutron scattering experiments. The instrument has been successfully applied to measure structure factors $S(\mathbf{Q})$ in liquids and amorphous materials, to collect full data sets of highly accurate structure factors for charge-density work, to measure the spin component of the ground-state magnetization in transition-metal and rare-earth compounds, to study the diffuse scattering from stacking faults and dislocation loops in Si single crystals, and for the investigation of various aspects of structural phase transitions: critical scattering in $SrTiO_3$, oxygen order and stripe order in high-T_c materials. A crossed-beam technique allows for local studies of texture, internal strain and phase changes in the bulk of materials.

Keywords: high-energy synchrotron radiation; structural phase transitions; liquids; amorphous materials.

1. Introduction

Synchrotron radiation with energies above ~80 keV interacts only weakly with matter. Since the mean free path is of the order of several millimetres, bulk properties of large crystals can be studied and there are no window problems associated with samples being mounted in cryostats or furnaces. In most cases the electron binding energies in atoms are much smaller than 80 keV, so that no resonance scattering occurs. Extinction effects in Bragg diffraction in imperfect single crystals are weak, *i.e.* only small corrections to first-order Born approximations are necessary in the interpretation of diffraction data. Bragg angles are of the order of a few degrees and crystals are studied in transmission geometry. The small Bragg angles lead to polarization factors close to unity also in the horizontal. Because of the short wavelength of the synchrotron radiation in use, diffraction experiments can be performed up to very high momentum transfers.

High-energy synchrotron X-ray diffraction is considered a new probe in condensed matter research because it combines the high penetration power of thermal neutrons with the extreme momentum space resolution achieved in modern X-ray diffraction experiments. In addition, the information content is strongly enhanced when the results from triple-crystal diffraction work using high-energy synchrotron radiation are combined with results obtained from neutron scattering experiments performed on the same sample, because of the basic difference in the intrinsic cross sections between the two techniques. Advantage can also be taken of the possibility of combining high momentum space resolution with high-energy resolution achieved in inelastic neutron scattering experiments, again using the same samples with both techniques.

The first triple-crystal diffractometer for high-energy synchrotron radiation was built at the National Synchrotron Light Source (NSLS) at Brookhaven National Laboratory and was first used at CHESS, Cornell Uni-

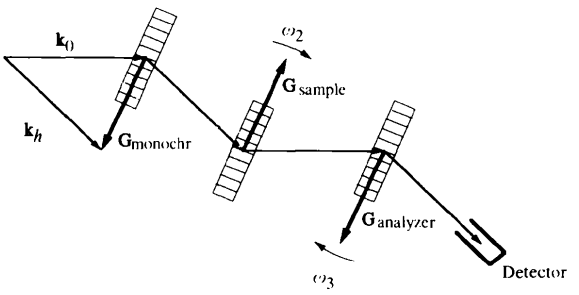

Figure 1
Schematic drawing of a triple-crystal diffractometer for high-energy synchrotron radiation. In reality, the Bragg angles are only of the order of 2°. The monochromator crystal diffracts the wavevector $\mathbf{k}_h$ out of the white divergent incident beam. The sample and analyser crystals can be tilted so that arbitrary scans through the scattering distribution in reciprocal space are possible. ω_1 represents the angle of rotation of the monochromator, ω_2 that of the sample and ω_3 that of the analyser crystal.

† Present address: Materials Department, Risø National Laboratory, DK-4000 Roskilde, Denmark.

versity (Hastings *et al.*, 1989). The layout in principle of such diffractometers for a non-dispersive setting is shown in Fig. 1. The corresponding **k**-space geometry in the scattering plane is indicated in Fig. 2. The resolution of such an instrument has been discussed by Neumann *et al.* (1994) and by Rütt *et al.* (1995). In non-dispersive setting the resolution in the scattering plane in the direction parallel to the reciprocal-lattice vector **G** is $\Delta q_x \simeq 2 \times 10^{-4}$ Å^{-1}, and $\Delta q_y \simeq 10^{-5}$ Å^{-1} in the direction perpendicular to **G** for silicon 111 and 80 keV synchrotron radiation. The asymmetry of the resolution in the scattering plane is due to the fact that the wavevectors $\mathbf{k}_0$ and $\mathbf{k}_h$, representing the incident and the Bragg diffracted beams, are about 20 times longer than the reciprocal-lattice vector **G**. The resolution perpendicular to the scattering plane, as determined by the detector aperture, is of the order $\Delta q_z \simeq 10^{-1}$ Å^{-1}.

For 100 keV synchrotron radiation the full width at half maximum (FWHM) of the diffraction pattern of a perfect silicon single crystal is typically of the order of a few tenths of an arcsecond. Therefore, the triple-crystal diffractometer must allow rotations of monochromator, sample and analyser crystals in steps of <0.1 arcsec. The long-term stability of the relative inclination of the analyser with respect to the monochromator crystal should also be better than 0.1 arcsec. In order to make full use of the fact that the same sample can be studied with neutrons and by means of triple-crystal diffractometry using high-energy synchrotron radiation, the sample stage should be able to carry heavy cryostats or furnaces as used on neutron spectrometers.

The outline of the paper is as follows. After a description of the high-field wiggler installed at the DORIS III storage ring and the HASYLAB high-energy wiggler beamline BW5, the design of the triple-crystal diffractometer, the optical control system for long-term stability and the performance of the diffractometer will be discussed. Finally, a number of typical applications are presented.

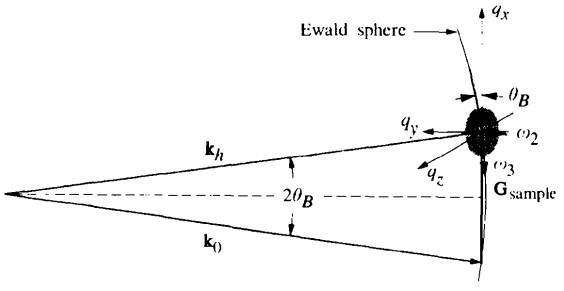

Figure 2
Scattering geometry in reciprocal space for a triple-crystal diffractometer for high-energy synchrotron radiation. $\mathbf{k}_0$ and $\mathbf{k}_h$ represent the wavevectors for the incident and the diffracted beams (k = 51 Å^{-1} for 100 keV photon energy). **G** is the reciprocal-lattice vector (G = 3.3 Å^{-1} for silicon 220). Scanning the sample corresponds to a transverse scan. Tilting the analyser corresponds to a movement along the Ewald sphere. Because of the small Bragg angles of about 2°, an analyser scan differs by only a little from a longitudinal scan.

Table 1
Parameters of the DORIS III high-field hybrid wiggler.

Period length	226.0 mm
Maximum field at 20 mm gap	2.0 T
Maximum K value	33.0
Number of poles	34.0
Device length	4.0 m
Magnet dimensions	
Length	77.7 mm
Width	130.0 mm
Height	217.4 mm
Volume	2187.0 cm^3
Weight	16.6 kg
Pole dimensions	
Length	35.3 mm
Width	90.0 mm
Height	189.4 mm
Overstand	2.0 mm
Chamber	2 × 2 mm^2
Permanent field, B_r	~1.15 T
Maximum operating temperature	333 K
Total weight of magnet material	1100.0 kg
Total power	198 W mA^{-1}
Power density	130 W mA^{-1} mrad^{-2}
E_c (DORIS at 4.5 GeV)	27 keV

2. High-field wiggler at the DORIS III storage ring

The storage ring DORIS was originally built for high-energy physics experiments and later used also as a source of synchrotron radiation. Since 1982, for two-thirds of the available beamtime, DORIS has been operated in colliding-beam mode at electron/positron energies of 5.3 GeV and used for synchrotron radiation experiments in parasitic mode. During the remaining time the storage ring was operated with different electron optics and an electron energy of 4.5 GeV for the production of synchrotron radiation in dedicated mode. From June 1993, the storage ring DORIS III, with seven new insertion-device beamlines, has been operated as a fully dedicated synchrotron radiation source. Since April 1994, the machine has been operated with positrons of 4.5 GeV energy. The horizontal emittance of the ring at that energy is 400 nmrad and the coupling is of the order of 3%. Most of the HASYLAB beamlines are optimized for angular flux. The high-field wiggler was designed to reach a critical energy close to the value for the bending-magnet radiation obtained when DORIS was operated at 5.3 GeV electron energy.

The parameters for the HASYLAB high-field wiggler HARWI 2 are presented in Table 1. For a detailed description of the device and its performance see Pflüger (1992, 1993, 1994). The permanent magnets in the hybrid structure are made of NdFeB. The strongest field achieved is 1.966 T at a gap of 20 mm. Fig. 3 shows the spectral angular flux of the HASYLAB high-field wiggler, and a comparison is made with the performance of the two insertion devices installed at the high-energy beamline ID15 at the ESRF.

3. HASYLAB high-energy beamline BW5

The parameters of the synchrotron radiation beam produced by the high-field wiggler are given in Table 2. At a

DORIS current of 100 mA, the total beam power is approximately 20 kW. The corresponding power density of 13 kW mrad^{-2} required several changes in beamline design as compared with the other HASYLAB wiggler beamlines. Fig. 4 shows the beamline layout in the horizontal plane. For a more detailed description of the beamline and its key components, see Hahn (1993). Owing to the high magnetic field, the wiggler emits radiation in a wide horizontal fan of opening angle 7.5 mrad, whereas presently only approximately 0.3 mrad are used at the experimental station. Therefore, at a distance of 10 m from the wiggler the beam is collimated from a width of ~80 mm down to ~20 mm. The device has to take up ~15 kW of synchrotron radiation power, which is absorbed by two 1 m-long water-cooled Cu plates. The radiation hits the plates at an angle of under 3°, thus reducing the power density by about a factor of 20. At a distance of 24 m from the wiggler, a second collimator, made of Cu and W with an aperture of 50 mm diameter, is installed. The water-cooled Cu collimator absorbs the radiation power, and the W collimator reduces the *bremsstrahlung* background in the experimental hutch. At 15 m from the source the beam

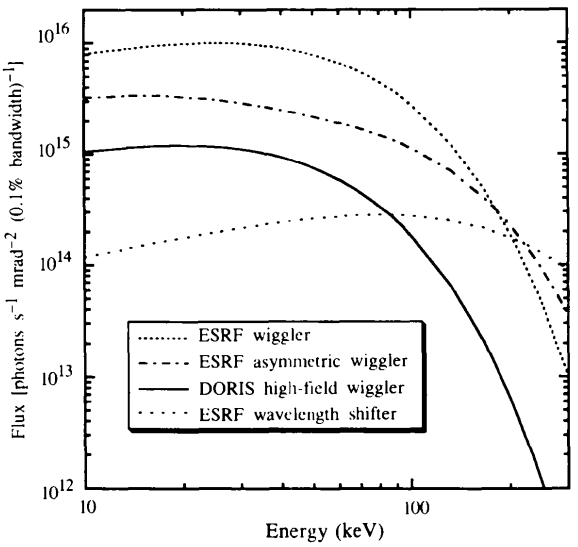

Figure 3
Comparison of the angular flux spectra of the HASYLAB high-field wiggler (DORIS operated at 4.5 GeV, 100 mA) and the asymmetric wiggler and the wavelength shifter installed at the high-energy beamline ID15 at the ESRF (6 GeV, 200 mA). For completeness, a comparison with the angular flux obtained with a standard ESRF wiggler (B = 1.25 T, 36 periods, 12.5 cm period length) is also shown.

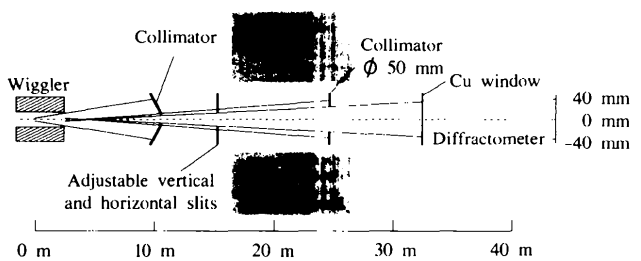

Figure 4
Layout of the HASYLAB high-energy wiggler beamline BW5. The first water-cooled collimator is located at a distance of 10 m from the source and reduces the beam width from ~80 to ~20 mm. For safety reasons a second water-cooled copper collimator combined with a tungsten collimator of 50 mm diameter aperture is located at 24 m from the wiggler. Water-cooled horizontal and vertical slit systems at 15 m from the wiggler allow the definition of the beam cross section. The beamline is terminated by a 1.5 mm-thick copper window, which strongly absorbs photons with energies below 50 keV.

Table 2
Electron- and photon-beam parameters for the high-field wiggler beamline BW5 at the DORIS III storage ring.

$\alpha = -0.5\beta'$, β' is the derivative of β; D describes the deviation, Δx, of the electron path from the ideal orbit, due to a deviation of its energy, ΔE, from the nominal value E_0: $\Delta x = D_x \Delta E/E_0$, D' is the derivative of D.

Electron beam		
Energy		4.5 GeV
Energy spread	τ_e	1.08×10^{-3}
Emittance	ε_{hor}	404.0 nmrad
	ε_{vert}	12.0 nmrad
β-function	β_{hor}	24.148 m rad^{-1}
	β_{vert}	8.706 m rad^{-1}
α-function	α_{hor}	−0.052
	α_{vert}	−0.068
Dispersion	D_{hor}	−0.312 m
	D_{vert}	0.000 m
	D'_{hor}	−0.112
Photon beam		
Source size	σ_{hor}	3.141 mm
	σ_{vert}	0.325 mm
Angular divergence	σ'_{hor}	0.177 mrad
	σ'_{vert}	0.0374 mrad

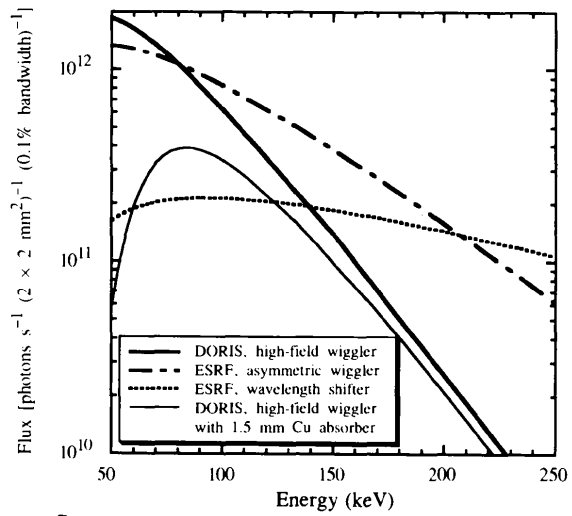

Figure 5
Spectral flux at the HASYLAB high-field wiggler beamline BW5 through an aperture of 2 × 2 mm^2 at a distance of 37 m from the source, with DORIS operated at 4.5 GeV and a current of 100 mA. Plots are calculated with 4 mm Al in the beam path, as well as for the case of an additional 1.5 mm Cu window in the beam. For comparison with the high-energy beamline ID15 of the ESRF (6 GeV, 200 mA), the spectral flux through a 2 × 2 mm^2 aperture at 63 m from the source calculated for the asymmetric wiggler and the wavelength shifter with 3.5 mm of Be and 4 mm Al in the beam is also shown.

cross section can be defined by water-cooled vertical and horizontal slit systems. The beamline is terminated by a 1.5 mm Cu window strongly absorbing the synchrotron radiation with energies below 50 keV, thereby protecting the monochromator crystal against heat load.

Fig. 5 shows the spectral flux of the HASYLAB high-field wiggler through an aperture of 2 × 2 mm^2 at a distance of 37 m from the source, *i.e.* at the entrance slit of the triple-crystal diffractometer in the experimental hutch. It turned out that this is the most appropriate quantity for optimizing almost all diffraction experiments performed at this beamline. For comparison, Fig. 5 also shows the analogue quantities for the high-energy beamline ID15 at the ESRF when operated at 6 GeV and 200 mA, *i.e.* for a 2 × 2 mm^2 aperture at a distance of 63 m from the source. For both beamlines the absorbing material in the beam has been included in the calculation, *i.e.* 4 mm Al plus 1.5 mm of Cu for BW5 at HASYLAB, and 3.5 mm Be plus 4 mm Al for ID15 at the ESRF. For reasons of comparison, the BW5 spectrum is also shown without absorption by the Cu filter. For some experiments the higher-order contamination of the incident beam has to be kept as small as possible and an increase of the magnetic gap of the wiggler can be of advantage. Fig. 6 shows the variation of the spectral flux through a 2 × 2 mm^2 aperture for different wiggler gaps. As an example, the intensity ratio of 80–240 keV radiation is about 100 for a magnetic gap of 20 mm and 2000 for a 40 mm gap, while the induced intensity loss at 80 keV is only by a factor of three.

4. Triple-crystal diffractometer at beamline BW5

Fig. 7 shows schematic diagrams of the triple-crystal diffractometer now in operation at HASYLAB beamline BW5. The scattering plane of the diffractometer was chosen to be horizontal as Bragg angles are of the order of a few degrees and the polarization factor is therefore always close to unity. In addition, a horizontal scattering plane facilitates the mounting of heavy equipment such as cryostats, furnaces or high-pressure cells on the sample stage.

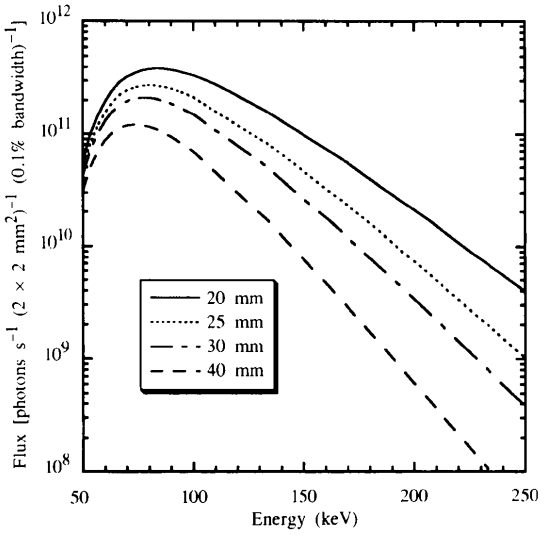

Figure 6
Spectral flux at the HASYLAB wiggler beamline BW5 through an aperture of 2 × 2 mm^2 at a distance of 37 m from the source, calculated for different heights of the magnetic gap of the wiggler. By varying the gap, the intensity ratio of first to higher harmonics in the beam incident on the sample is tunable.

The diffractometer components are mounted on three base plates. The first base plate is made of granite, of dimensions 3200 × 1200 × 120 mm, and carries the monochromator, sample and analyser towers, as well as the beam-defining slit system. The slit system consists of a 400 mm-long steel collimator with an aperture of 6 × 6 mm, which is mounted on a stage with a rotational and a translational degree of freedom perpendicular to the beam direction for proper alignment. In the middle of the steel collimator, 5 mm-thick tungsten plates with the appropriate aperture can be inserted. The collimator is mounted in a vacuum in order to reduce background radiation and to prevent ozone production. The whole beam-defining system is surrounded by heavy lead shielding mounted independently on the floor, leaving some freedom for movements of the collimator as needed for alignment purposes. The towers for monochromator, sample and analyser crystals are mounted on air cushions, so that the distance between them can be adapted to the needs of specific experiments. For purposes of alignment and in order to fix the scattering angles, all towers can be moved on rails perpendicular to the direction of the incident beam. In order to optimize the peak-to-background ratio, a number of adjustable and fixed slit systems, as well as collimators, are mounted between the crystals and in front of the detector on 'Physics Instruments' guides. When scattering angles are changed, these guides, and thereby the slits and collimators, will follow the beam path automatically, due to a mechanical guiding system. A scintillation counter serves to monitor the intensity of the monochromatic beam by measuring the Compton scattering from a thin Al foil. The counter is mounted on the Physics Instruments guide between the monochromator and sample towers together with an automatic shutter for protection against count-rate overload in the detector. Between sample and analyser a combination of steel collimators and a wheel with calibrated absorbers is mounted, allowing for a dynamic range of 11 orders of magnitude in the intensities measured with the Ge solid-state detector. This detector is mounted on the second base plate on a translational table allowing a displacement in the direction perpendicular to the incident beam of up to 1600 mm. Again, proper mechanical guidance assures that the adjustable slit and the steel collimator are directed towards the diffracted beam. Whereas monochromator, sample and analyser crystals have to be mounted on a common granite base plate for stability reasons, the detector can be mounted on a separate plate because the accuracy needed for its positioning scales with the aperture of the slit in front of the detector, which in general is a couple of mil-

limetres wide. Both base plates are mounted on three-point bearings on steel frames which are positioned by means of three air cushions on the floor. The three-point bearings contain motor-controlled lifting devices so that both base plates can be tilted and lifted independently for alignment purposes. The third base plate carries the CCD camera and is fixed on a concrete wall needed for shielding at the back of the experimental hutch.

4.1. *Monochromator*

Up to four crystals can be mounted without cooling on a (χ,φ)-circle segment on top of a rotary table. The crystals are fixed on a translational table, allowing a change of crystal without opening the monochromator tank, which is under He atmosphere, and thus without removing the heavy shielding around it. If $\Delta\alpha$ is the FWHM of the horizontal divergence of the incident beam and $\Delta\omega_1$ the FWHM of the diffraction pattern of the monochromator crystal, the wavelength band $\Delta\lambda/\lambda$ selected by the monochromator is calculated in the limit of small Bragg angles according to

$$\Delta\lambda/\lambda = \cot(\theta_B)(\Delta\alpha + \Delta\omega_1). \quad (1)$$

θ_B represents the Bragg angle. For 100 keV photons diffracted at Si (220), one obtains $\Delta\lambda/\lambda = 0.006$ for a perfect crystal and $\Delta\lambda/\lambda = 0.008$ for an imperfect crystal, with $\Delta\omega_1 = 10$ arcsec. The relatively large values of $\Delta\lambda/\lambda$ are due to the small Bragg angles, which obviously are a disadvantage if beams with a narrow energy band are needed. However, in most of the diffraction experiments performed so far at beamline BW5, a bandwidth of the order of 1% could be tolerated. In cases when better energy resolution is needed, the angular divergence of the incident beam can be reduced by reducing the width of the slits in the slit system in the tunnel at 15 m from the wiggler. For studies of imperfect sample crystals and/or diffuse scattering, important gains in intensity can be obtained without losing resolution by using imperfect single crystals as monochromators. Besides perfect silicon crystals, the following monochromator crystals are presently in use at BW5: annealed Si with $\Delta\omega_1 \leq 10''$ (Schneider *et al.*, 1988, 1989), $SrTiO_3$ crystals with $\Delta\omega_1 \simeq 40''$ and $SiTaSi_2$ crystals with $\Delta\omega_1 \simeq 100''$ (Neumann *et al.*, 1996). The intensities at the sample obtained for a 2×2 mm^2 beam of 100 keV photons range from 1×10^{10} to 8×10^{11} s^{-1}. The degree of linear polarization for full vertical integration of the beam was determined to be 81(3)% from an analysis of $S(\mathbf{Q})$ measurements on liquids. However, because of the small Bragg angles, this is in general not a critical quantity.

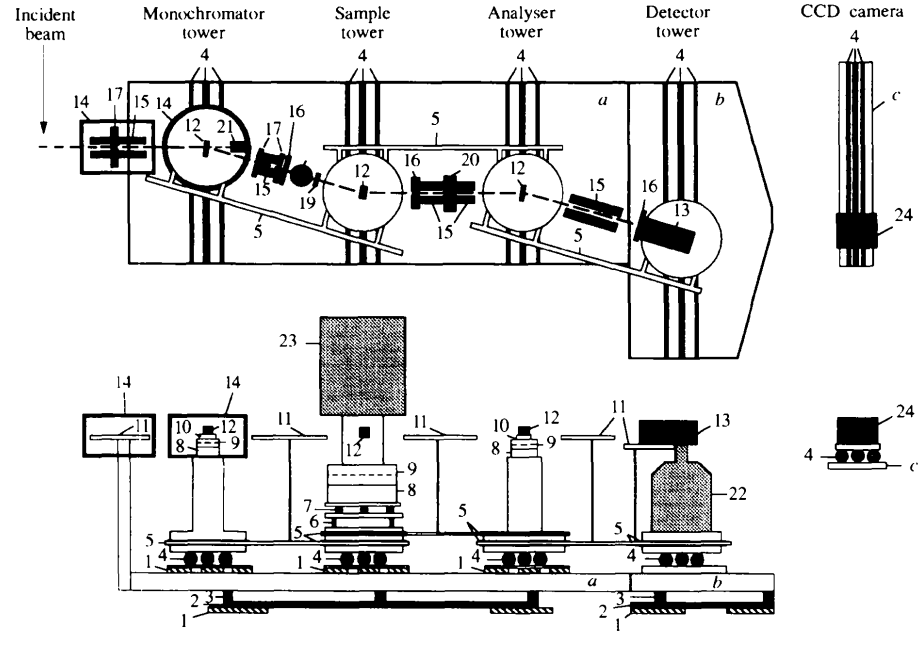

Figure 7
Layout of the triple-crystal diffractometer. The base plates, (*a*) and (*b*), are mounted on three-point bearings (3) fixed on a steel frame (2) positioned *via* air cushions (1) on the floor. Monochromator, sample and analyser towers are mounted on rails (4); their mutual distance can be adapted to the experimental needs by means of air cushions (1) on the granite plate (*a*). Mechanical guidances (5) transform the linear movements of the towers into rotations. Monochromator and analyser crystals (12) are mounted on a rotary table (8), a (χ,φ)-circle segment (9) and a translational table (10) for on-line change of crystals. The rotary table (8) for the analyser is connected to a Heidenhain angular encoder. The sample stage consists of vertical (6) and horizontal (7) degrees of freedom, a large rotary table (8) and a heavy (χ,φ)-circle segment (9) on which the sample crystal (12) can be mounted in large cryostats (23). Physics Instruments rails (11), which automatically follow the tower movements, allow mounting of steel collimators (15), adjustable (16) and fixed (17) slit systems, a monitor counter (18), an automatic protection of the detector against count rate overload (19), and an absorber wheel (20). The beam-defining slit system and the monochromator crystal, as well as the beamstop (21), are surrounded by heavy lead and steel shielding (14). The Ge detector (13) is also well shielded. Because of the large Dewar (22), liquid nitrogen has to be refilled once a week. At the back of the experimental hutch a CCD camera (24) is fixed on rails (4) mounted on a steel plate (*c*).

4.2. *Analyser*

The design of the analyser tower is identical to that of the monochromator, except for the shielding vessel. For all the different types of monochromators mentioned above, corresponding analyser crystals exist. Because of the extreme sensitivity of the analyser position to the location of the scan volume in reciprocal space, the ω_3 rotary table is equipped with a Heidenhain angular encoder with a precision of ± 0.04 arcsec.

4.3. *Sample stage*

Because samples are often mounted in heavy cryostats or furnaces, the sample stage can carry weights up to about 500 kg. From the bottom to the top the sample tower contains a lifting table (± 30 mm) and a table for horizontal translations perpendicular to the incident beam (± 70 mm). Next, a Huber 430 rotary table and a massive Franke and Heidrich (χ,φ)-circle segment ($\pm 15^\circ$) are mounted, on which, for example, an ILL 'Orange' He cryostat can be positioned, which reaches temperatures down to 2 K. A furnace, reaching temperatures up to 1673 K, is also available. If all rotational degrees of freedom are needed for sample orientation, the ensemble of the rotary table and the (χ,φ)-circle segment is replaced by a Huber Eulerian cradle mounted on another rotary table. The φ axis in the Eulerian cradle is offset such that a two-stage closed-cycle refrigerator can be mounted, which reaches temperatures down to 10–15 K. Both cryostats have cylindrical heat shields of large diameter to avoid powder lines entering the detector. For measurements of the static structure factor of liquids and amorphous materials, an evacuated scattering chamber of 500 mm diameter can be mounted on the sample stage. It allows measurements up to a momentum transfer of $Q = (4\pi/\lambda)\sin\theta_B = 32$ Å^{-1}.

4.4. *Detectors*

An intrinsic Canberra Ge detector (crystal 15 mm thick and 25.5 mm in diameter) is mounted on top of a 30 l Dewar and shielded well by steel and lead. In general, background count rates are less than 1 count s^{-1}. The detector works in its linear regime up to count rates of the order of 6×10^4 counts s^{-1}. Using a fast spectroscopy amplifier (Canberra 2024) the experimentally verified dead time for a monochromatic beam of 100 keV photons is 2.1 μs and the resolution at that energy is ~550 eV for low count rates. The energy spectrum can be recorded by means of a LeCroy ADC 3512. Three Ortec 551 single-channel analysers allow simultaneous measurement of scattered photons of the fundamental and higher harmonics. A 253×200 mm^2 image plate can be mounted in front of the Ge detector and allows, after removal of the collimators and the absorber wheel between sample and detector, the simultaneous determination of the scattering angles for several Bragg reflections. This information can, for example, be used to establish the orientation matrix of the sample. Exposure times for this purpose are of the order of 10–30 s. A modified XIOS-II camera from Photonics Science, a 12-bit tapered fibre-optics CCD with an area of 77×83 mm^2, is mounted on a rotary table and a translational table; the whole ensemble is mounted on the third base plate fixed at the concrete beamstop.

5. Electronic hardware and computer software

Up to 48 stepping motors are connected according to HASYLAB standards *via* CAMAC to a MicroVAX computer operating under VMS. Again following HASYLAB standards, the software for motor controls, counting and visualization of data is based on the *SPECTRA* program package (Kracht, 1994). The existing software provides a guide for diffractometer alignment and energy calibration, and allows for automatic centring of reflections and calculation of orientation matrices, as well as azimuthal scans and arbitrary scans in momentum space (Kracht & Poulsen, 1995). Special scan modes, *e.g.* automatic measurements of superlattice reflections as a function of temperature, can be implemented *via* macros. For automatic data collection in four-circle mode, the *DIF4* software package (Eichhorn, 1993) is installed, which is also in use at HASYLAB diffractometers D3 and F1. *DIF4* contains all standard crystallography data-collection routines (automatic indexing and unit-cell determination, orientation matrix refinement and Bravais lattice determination, refinement of cell constants) and allows for on-line data reduction, including checks on both intensity and peak positions of an arbitrary number of reference reflections.

6. Performance of the diffractometer

The diffraction pattern of a perfect crystal in symmetrical transmission geometry for negligible absorption is given by (*e.g.* Zachariasen, 1945)

$$R(\eta\omega) = 1/2[1 + (\eta\omega)^2],$$
$$\eta = 2/(\mathrm{FWHM})_{\mathrm{dyn}} = \pi V_c \sin(2\theta_B)/r_0\lambda^2 F_H. \qquad (2)$$

ω represents the crystal rotation angle, V_c is the unit-cell volume, r_0 is the classical electron radius and F_H is the structure factor for reflection **H**. $(\mathrm{FWHM})_{\mathrm{dyn}}$ represents the full width at half maximum of the diffraction pattern calculated for a perfect crystal by means of dynamical theory, which amounts to 0.37″ for Si(220) and 100 keV photons. It is interesting to note that $(\mathrm{FWHM})_{\mathrm{dyn}}$ decreases proportionally with wavelength, λ, while the intensity in the wings of the diffraction pattern even decreases proportionally with λ^2. Fig. 8 shows the result of a central analyser scan performed with three perfect Si crystals mounted in a dispersion-free (+, −, +)-setting. 100 keV radiation was diffracted at 220 reflections in a symmetric transmission geometry. The thickness of the crystals was 1 cm each. The experimental data are in very good agreement with the theoretical diffraction pattern

calculated according to Neumann *et al.* (1994),

$$I(\omega_2, \omega_3) = \int d\alpha \int d(\Delta\lambda) F(\alpha) J(\Delta\lambda) R_M(\alpha - \delta) \times R_S[\omega_2 - b_1(\alpha - \delta)] \times R_A\{-\omega_2 + \omega_3 - b_2[\omega_2 - b_1(\alpha - \delta)]\} \quad (3)$$

with

$$b_i = \sin(\theta_B - \varphi_i)/\sin(\theta_B + \varphi_i).$$

ω_2 and ω_3 are the rotation angles of the sample and analyser crystals (Fig. 1). $J(\Delta\lambda)$ denotes the spectral and $F(\alpha)$ the angular distribution function of the primary synchrotron radiation beam. R_M, R_S and R_A represent the theoretical diffraction patterns from monochromator, sample and analyser crystals. $\delta = (\Delta\lambda/\lambda)\tan\theta_B$ describes the change in the Bragg angle if the wavelength is changed by $\Delta\lambda$ with respect to the reference setting. b_i is the asymmetry parameter, with φ_i being the angle between the net planes and the surface normal of the crystal. The fitted value of FWHM = 0.56″ is only 0.02″ larger than the theoretical value calculated under the assumption of ideally perfect monochromator, sample and analyser crystals.

The long-term stability of the relative orientations of monochromator and analyser crystals is crucial, especially for accurate determinations of lattice parameters by means of analyser scans. In order to correct for possible deviations due to temperature fluctuation or other mechanical drifts, two electronic autocollimators were installed. They can measure absolute rotations of the towers with an accuracy of ~0.01 arcsec. Mirrors are fixed on the towers and the autocollimators are positioned on an additional vibration-attenuated granite plate. Assuming the mechanical connection between the mirrors and the corresponding crystals to be rigid, the only remaining inaccuracy in the angular setting of the crystals could arise from inaccurate positioning of the rotary tables. These are therefore controlled by angular encoders with an accuracy of ~0.1 arcsec. To test the effect of temperature fluctuations on the crystal orientations, the temperature in the experimental hutch was increased by 2 K. As a result, the monochromator tower was tilted by about 1 arcsec. However, as shown in Fig. 9, the relative change in the orientation of monochromator and analyser crystals was much smaller, and, from 30 min after the temperature change and onwards, the relative angle was stable with an accuracy of about 0.1 arcsec over 13 h. As a consequence, air conditioning was installed in the experimental hutch. It keeps the temperature constant within ±0.2 K and the optical control system is therefore no longer needed.

For most applications the scattering is discussed in **k** or momentum space, instead of angle space (ω_2, ω_3). For the tilt directions and **q** coordinates shown in Fig. 2, the transformation from one space into the other is performed

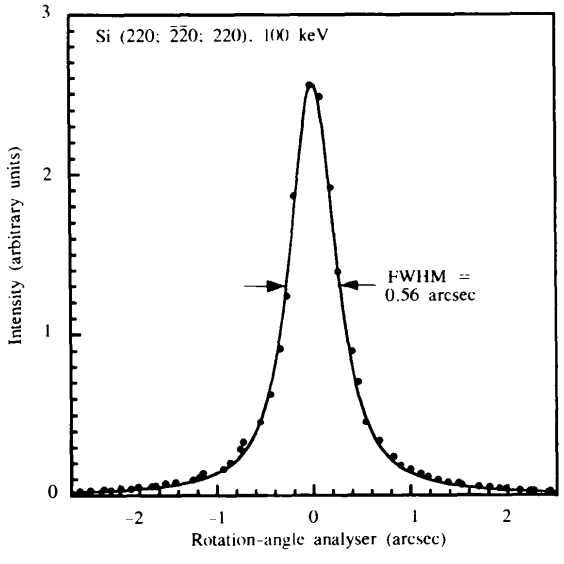

Figure 8
Central analyser scan (ω_2 = 0, ω_3 scanned) for a non-dispersive (+, −, +) set-up with three perfect silicon crystals diffracting in symmetrical transmission geometry from (220) planes. The experimental data (dots) are in excellent agreement with the theoretical intensity distribution calculated with diffraction patterns for perfect crystals from dynamical theory; the experimental FWHM agrees almost exactly with the theoretical value of 0.54 arcsec.

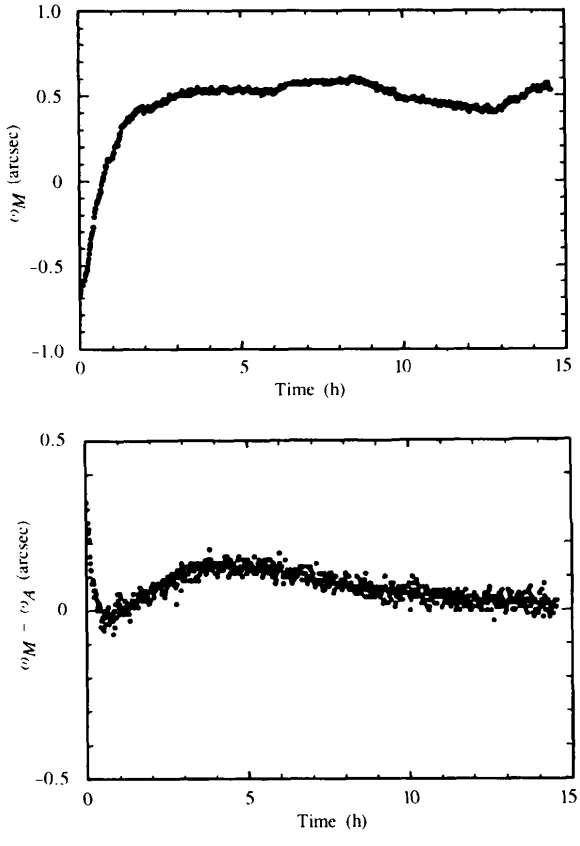

Figure 9
Angular stability of the monochromator *versus* analyser tower measured with two optical autocollimators after a change of the temperature in the hutch of 2 K. The induced tilt of the monochromator tower was ~1.2 arcsec; the maximum relative tilt was ~0.4″. After 30 min the relative angular stability of the two towers is of the order of 0.1″.

by the following equations,

$$q_x = -|\mathbf{k}|\cos(\theta_B)\omega_3, \qquad q_y = |\mathbf{G}|(\omega_2 - \omega_3/2). \quad (4)$$

Without going into detail, the main features of the resolution function of the triple-crystal diffractometer for high-energy synchrotron radiation in non-dispersive setting can be seen from fictitious analyser and sample central scans assuming

$$q_x \simeq -|\mathbf{k}|\omega_3, \qquad q_y \simeq |\mathbf{G}|\omega_2. \quad (5)$$

$\cos\theta_B$ has been put equal to unity because of the small Bragg angles, θ_B. For the analyser (longitudinal) scan we assume δ-function-shaped diffraction patterns for monochromator and sample; for the sample (transverse) scan the diffraction patterns of monochromator and analyser are assumed to be δ-functions. The FWHMs of these scans can then be calculated from (2) and (5) as

$$(\mathrm{FWHM})_{\mathrm{longitudinal}} = 8\pi r_0 F_H / V_c |\mathbf{G}|,$$
$$(\mathrm{FWHM})_{\mathrm{transverse}} = 8\pi r_0 F_H / V_c |\mathbf{k}|. \quad (6)$$

To a good approximation, the FWHM of a longitudinal scan is independent of the wavelength of the diffracted radiation but becomes smaller with higher momentum transfer, **G**, *i.e.* the longitudinal resolution improves for higher-order reflections. On the other hand, the FWHM of a transverse scan is essentially independent of momentum transfer but decreases with increasing wavevector, **k**, *i.e.* with decreasing wavelength of the diffracted radiation. In both cases the FWHMs decrease with decreasing structure factors, *i.e.* they become smaller for weak reflections.

7. Applications

In this section, typical applications of the triple-crystal diffractometer at the high-field wiggler beamline BW5 are sketched.

The use of high-energy photons for diffraction studies on disordered materials was first suggested by Egelstaff (1983), but, to the authors' knowledge, only one experiment has been performed along these lines using γ-rays from radioactive sources (Root *et al.*, 1986). With the advent of modern synchrotron radiation facilities providing high-intensity beams of X-rays at energies above 80 keV, the idea saw a revival (Neuefeind & Poulsen, 1995). The main advantages of using high-energy synchrotron radiation for measurements of the static structure factor $S(\mathbf{Q})$ are the large accessible Q range and the low absorption. Moreover, systematic corrections are low (Poulsen & Neuefeind, 1995). Fig. 10 shows raw data taken for molten $ZnCl_2$ at 623 K with 100 keV radiation in a low-Q set-up (Neuefeind *et al.*, 1998). The empty-can measurement can be subtracted from the data; however, the regions where the powder lines from the steel cylinder with 9 mm outer and 7 mm inner diameter occur have to be excluded from any further consideration. The structure factors measured with 100 keV photons and neutrons (Allen *et al.*, 1991) show strong differences because of the difference in the intrinsic cross sections involved in the scattering. The measurements on molten $ZnCl_2$ presented in Fig. 11 indicate the gain in information on the partial pair-distribution functions which can be expected from a combination of neutron and high-energy synchrotron radiation data. Published work discusses the bond angle distribution in amorphous germania and silica (Poulsen *et al.*, 1995; Neuefeind & Liss, 1996) and the atomic and electronic structure of liquid *N*-methylformamide (Neuefeind *et al.*, 1996).

Recently, two data sets of structure factors up to $\sin\theta/\lambda = 1.4$ Å^{-1} have been measured on a Cu_2O single crystal, 190 μm in diameter, in automatic four-circle data-collection mode using 100 keV synchrotron radiation from an annealed Si(111) monochromator (Lippmann & Schneider, 1996). The first data set consists of 710 reflections (169 unique), which were recorded in conventional ω-step scan mode in about 2 d. The second data set included 1535 reflections (130 unique), which were measured in about 2.5 d using the continuous-scan mode, *i.e.* the detector was enabled when ω rotations of the sample were performed. Absorption and extinction effects are very weak and internal consistencies $R(|\mathbf{F}|^2)$ of 0.64% for the first and 0.38% for the second data set were achieved, demonstrating the high quality of the data sets. A multipole model was refined down to an agreement factor of 0.69% [$wR(F) = 0.90\%$, goodness of fit = 1.16]. The refined results compare favourably with earlier results obtained using the HASYLAB diffractometer D3 with 0.56 Å (22 keV) radiation by Kirfel & Eichhorn (1990). These results demonstrate the potential of accurate structure-factor measurements with high-energy synchrotron radiation for charge-density work or the determination of highly accurate structural parameters in systems undergoing structural phase transitions.

Synchrotron radiation opened the possibility of studying ground-state properties of magnetic materials. An outline

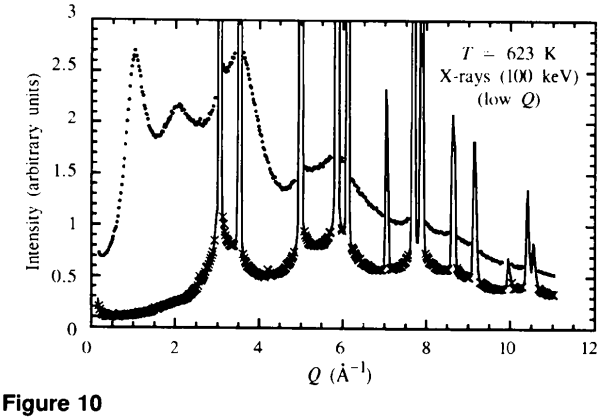

Figure 10
Structure-factor measurement with 100 keV radiation for molten $ZnCl_2$ at 623 K contained in a steel cylinder of 9 mm outer and 7 mm inner diameter (dots). The strong powder lines in the empty-can measurement (solid line) define 'dead' regions in momentum transfer Q; the crosses represent the points used in the further data processing.

of the theory has been given by Blume & Gibbs (1988). If such measurements are performed with high-energy synchrotron radiation, *e.g.* on antiferromagnetic ordered systems, only the spin component of the magnetic moment perpendicular to the scattering plane contributes to the scattering. All other components are projected out due to the small Bragg angles. In addition, large samples can be studied so that bulk properties are probed and a comparison can be made with neutron results obtained on the same sample. This offers another possibility of separating spin and orbit contributions to the magnetic moment. Fig. 12 shows the results of double-crystal scans at the 300 magnetic superlattice reflection of MnF_2 at saturation performed with 80 and 160 keV synchrotron radiation (Strempfer, 1997). The monochromator was an annealed Si crystal diffracting from (311) planes in an almost dispersion-free (+, −)-setting. A quick change to three-crystal mode of operation is straightforward. For more details on investigations of magnetic systems with high-energy synchrotron radiation, including the Q-dependence of the magnetic scattering and a discussion of the effect of multiple Bragg scattering, see Lippert *et al.* (1994) and Strempfer *et al.* (1996).

Full advantage of the high momentum space resolution of the triple-crystal diffractometer for high-energy synchrotron radiation has been made in a study of the defect scattering from annealed Czochralski-grown Si single crystals, which contain about 10 p.p.m. of O atoms. If these crystals are annealed at 1023 K, SiO_2 precipitates are created. Their size and number density can be determined by small-angle neutron scattering (Messoloras *et al.*, 1989). At temperatures above 1173 K, stacking faults on {111} lattice planes, as well as dislocation loops, are formed, which give rise to the diffuse scattering shown in Fig. 13 (Schmidt, 1992), measured on the same sample as used in the small-angle neutron scattering experiments. The contour plot shown has been calculated from a set of one-dimensional scans. One of the longitudinal scans is shown in Fig. 14. The two side peaks are due to the stacking faults. Their width is independent of the distance q_y from the reciprocal-lattice point, and a stacking-fault diameter was calculated using the theory of Larson & Schmatz (1980). The width of the peak in the centre, which is due to the dislocation loops, is q_y-dependent, and, after subtraction of the relatively large contribution of thermal diffuse scattering, a loop diameter of approximately 250 Å was calculated (Schmidt, 1995). The quantitative analysis of the diffuse scattering due to the dislocation loops is far more difficult than the characterization of the diffuse scattering from stacking faults. About 10 min are needed to perform a longitudinal scan such as the one shown in Fig. 14, and

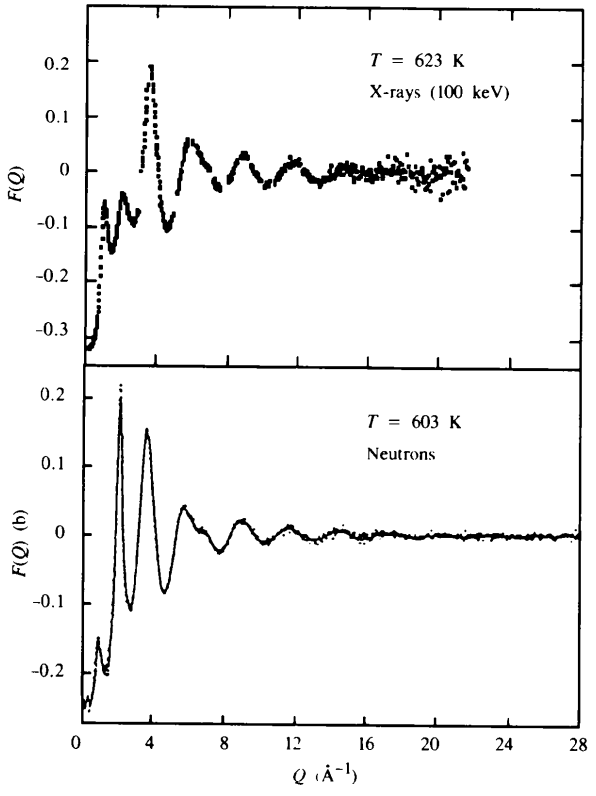

Figure 11
Structure factor of molten $ZnCl_2$ measured by means of 100 keV synchrotron radiation and thermal neutrons (Allen *et al.*, 1991). The synchrotron radiation data are subject to the usual corrections: $F(Q) = [I(Q) - \sum(f_i)^2 - \sum C_i]/\sum(f_i)^2$, where $I(Q)$ represents the scattered intensity normalized to constant monitor counts and corrected for deadtime effects, absorption and polarization (a correction for multiple scattering was not necessary). f_i is the atomic scattering factor and C_i represents the Compton-scattered intensity from atom i; the summation is over the unit composition. The difference between the two data sets at low Q demonstrates the potential of combining neutron and hard X-ray data for the determination of pair-distribution functions in amorphous and liquid systems.

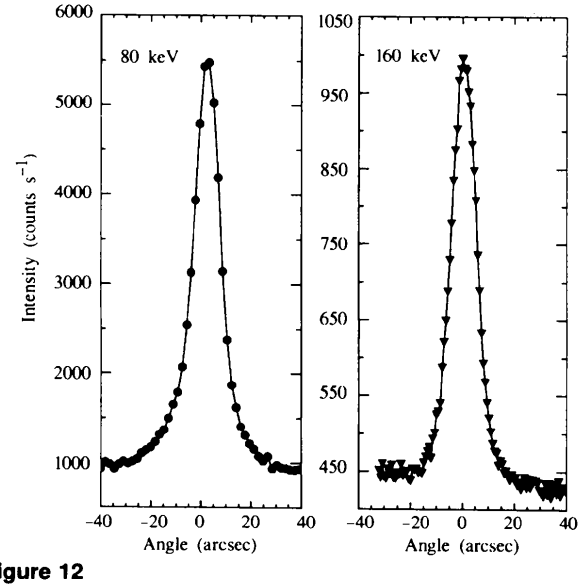

Figure 12
Transverse scans performed at the 300 magnetic superlattice reflection on MnF_2 at 4 K using 80 and 160 keV synchrotron radiation. An annealed Si crystal was used as monochromator in an almost dispersion-free double-crystal set-up. The full width at half maxima of the rocking curves are 12 and 10″, respectively. The magnetic reflection is about six orders of magnitude weaker than low-order charge reflections.

therefore meaningful *in-situ* studies of defect formation in Cz Si under annealing can be carried out at beamline BW5 (Schmidt, 1995).

Because large samples can be mounted easily in cryostats, triple-crystal diffractometers for high-energy synchrotron radiation are very well suited for studying structural phase transitions (Neumann, Poulsen *et al.*, 1995). The investigation of the sharp component of the critical scattering in $SrTiO_3$ above $T_c \simeq 100$ K, which is considered to be strongly affected by defects, is an instructive example, because the same sample, about 1 cm^3 in dimension, could be studied with X-rays and neutrons. As a result, it was shown that no sharp component exists in the bulk of the sample and that, as shown in Fig. 15, the temperature dependence of the inverse half-width of the Lorentzian-shaped critical scattering agrees very well with a calculation based on the inelastic neutron scattering data (Shirane *et al.*, 1993; Neumann, Rütt *et al.*, 1995). On the other hand, the high-resolution synchrotron radiation measurements have shown that the sharp component occurs in near-surface regions of the crystal (see inset of Fig. 15). In the meantime, systematic studies at the high-energy beamline of the PETRA undulator (Hahn *et al.*, 1997) revealed a direct correlation between the sharp component of the critical scattering in a layer at the sample surface of about 100 μm thickness and an increase in strain and mosaicity as well as with a gradient in the lattice parameter (Rütt, 1996; Rütt *et al.*, 1997).

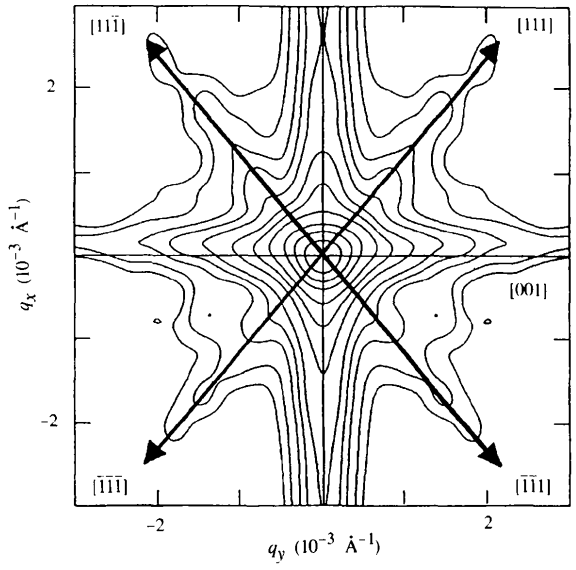

Figure 13
Diffuse scattering of 100 keV synchrotron radiation measured at room temperature in the vicinity of reflection 220 of a Czochralski-grown Si crystal annealed for 24 h at 1023 K and 20 h at 1323 K (Schmidt, 1992). The streaks along ⟨111⟩ are due to stacking faults on {111} planes with Burgers vector ⟨111⟩; the streaks along ⟨001⟩ are due to dislocation loops on {111} and {110} planes.

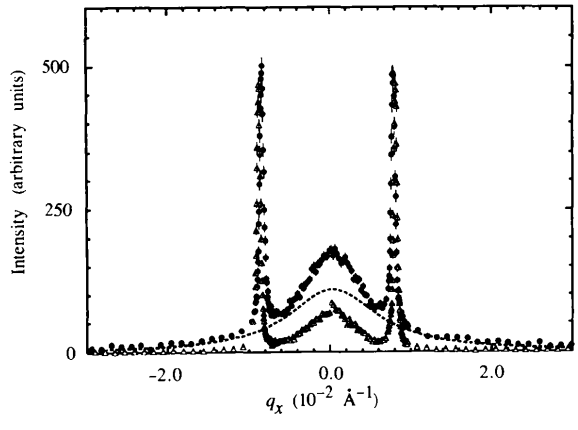

Figure 14
Longitudinal scans through the diffuse scattering shown in Fig. 13 at $q_y = 6 \times 10^{-3}$ Å^{-1} performed at room temperature (full dots) and 12 K (open triangles). The two sharp peaks are due to stacking faults; the wider peak in the centre is due to dislocation loops. The Lorentzian-shaped curve (dotted line) represents the calculated thermal diffuse scattering, which describes very well the difference between room- and low-temperature measurements (Schmidt, 1995).

In this context, reference should be made to recent work by Gibaud *et al.* (1997), who studied diffuse scattering from $KMnF_3$ at 200, 186 and 75 K by means of high-energy monochromatic Laue X-ray scattering using the X17B1 wiggler beamline at the NSLS at Brookhaven National Laboratory and an image-plate detector. Using 60 keV radiation, the measurements were not affected by strong fluorescence lines, and, because the Ewald sphere is flat,

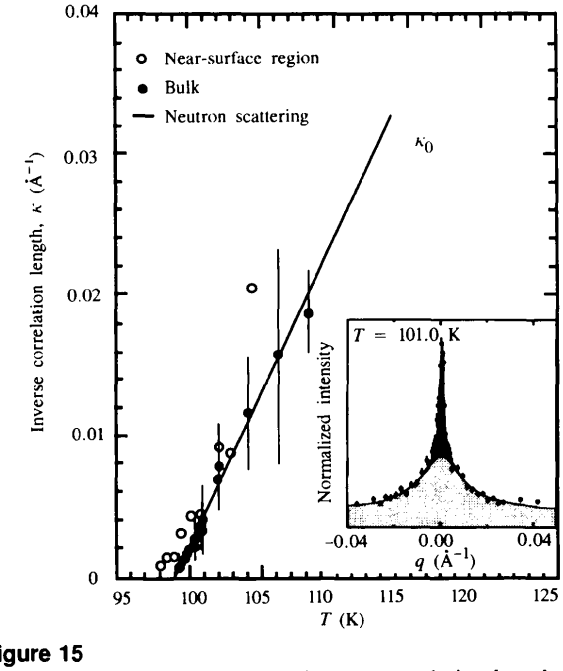

Figure 15
Temperature dependence of the inverse correlation length of the critical fluctuations in $SrTiO_3$ measured with 100 keV synchrotron radiation at reflection 0.5(511) above the critical temperature $T_c = 99.5$ K. In the bulk of the sample the result of neutron scattering experiments (solid line) was well reproduced. Only in near-surface regions was the additional sharp component in the critical scattering found (dark-coloured section in the inset) and the temperature dependence of the half-width of the Lorentzian-shaped critical scattering distribution was slightly different (open circles).

essentially only one plane in reciprocal space contributed to the scattering recorded on the image plate, performing $\pm 4^\circ$ oscillations of the sample. Exposure times as short as 150 s saturated the image plate at the Bragg peak locations and produced clearly visible diffuse patterns.

The momentum space resolution in single-crystal diffraction experiments on high-T_c superconducting materials is still limited by the perfection of the samples, and, at present, the intrinsic high resolution of a triple-crystal diffractometer for high-energy synchrotron radiation often is of no value. Therefore, $SrTiO_3$ crystals with a mosaicity of the order of 40 arcsec have been used as monochromator and analyser, increasing the intensity in the detector by approximately two orders of magnitude without losses in momentum space resolution. In this way, the Ortho-II superstructure of $YBa_2Cu_3O_{6.5}$, as well as the Ortho-III superstructure of $YBa_2Cu_3O_{6.77}$, could be studied with the best possible resolution obtainable with the present samples (Schleger, Hadfield *et al.*, 1995; Schleger, Casalta *et al.*, 1995). Compared with neutron studies of the same $YBa_2Cu_3O_{6.5}$ sample with worse resolution, an intensity gain of three orders of magnitude was achieved, and novel quenching experiments could be performed at the BW5 beamline. Work on $YBa_2Cu_3O_{6+x}$, with $x = 0.35$ and 0.36, is summarized by Poulsen *et al.* (1996). More recently, the charge scattering associated with stripe order has been measured in $La_{1.775}Sr_{0.225}NiO_4$ using 100 keV photons and $SiTaSi_2$ crystals both as monochromator and analyser (Vigliante *et al.*, 1997).

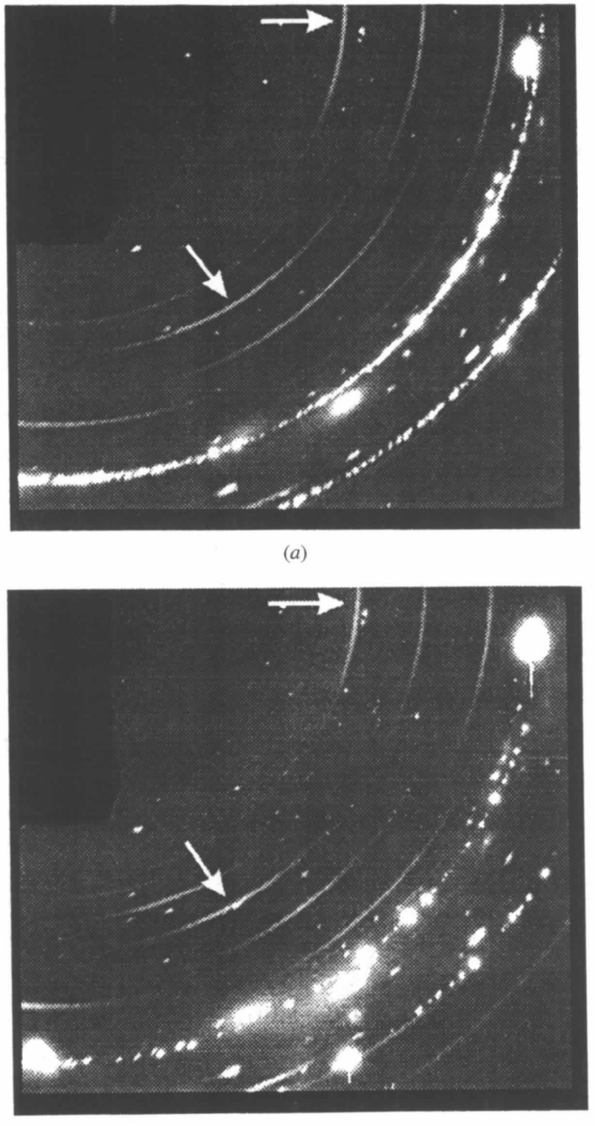

(*a*)

(*b*)

Figure 16
Diffraction images from a CCD detector recorded with 100 keV photons from a monofilament of Ag/(Bi, Pb)$_2$Sr$_2$Ca$_2$Cu$_3$O$_y$ superconducting tape before (*a*) and after annealing for 26 h at 1108 K. The superconducting grains are small and partly aligned. Hence, they give rise to small segments: in (*a*) the arrow marks diffraction from the Bi-2212 phase, in (*b*) the arrow indicates diffraction from the Bi-2223 phase. The silver is recrystallized and gives rise to dotted segments.

Some of the most promising applications of high-T_c superconductors are related to the use of wires and tapes of the (Bi, Pb)$_2$Sr$_2$Ca$_2$Cu$_3$O$_y$ material (abbreviated as the 2223 phase). Precursor powder, consisting mainly of the 2212 phase [(Bi, Pb)$_2$Sr$_2$CaCu$_2$O$_y$], is filled into Ag tubes, which are subsequently rolled and annealed, at temperatures between 1073 and 1123 K, several times. During this treatment, oxygen diffuses through the Ag sheet, the 2212 phase is transformed into 2223, and the superconducting grains grow and develop a strong *c*-axis alignment. The final tapes have cross sections of approximately 3 mm $\times$ 200 μm. The critical current density at 77 K is the crucial parameter to optimize, but in order to do so it may be necessary to determine what happens during the thermo-mechanical processing. By utilizing the penetration power of 100 keV X-rays, *in-situ* studies were performed recently, allowing a full structural description of the annealing process (Frello *et al.*, 1997; Poulsen *et al.*, 1998). An example of the raw data is given in Fig. 16. Using the CCD camera installed in the back of the experimental hutch (*cf.* Fig. 7), optimization of processing parameters has been performed based on the *in-situ* behaviour of some 60 tapes.

The potential of performing local studies in the bulk of materials by means of high-energy synchrotron radiation for materials science has been discussed recently by Poulsen *et al.* (1997). Using crossed-beam techniques, gauge volumes of 50 $\times$ 50 $\times$ 500 μm^3 have been achieved at BW5 (Garbe *et al.*, 1996). The long dimension of the gauge volume in the beam direction is due to the small Bragg angles. In a best-case scenario, minimum gauge volumes of 5 $\times$ 5 $\times$ 50 μm^3 seem obtainable. It thus becomes possible to measure non-destructively the fundamental microstructural parameters related to the individual grains in the material: crystallographic orientation, strain, size, dislocation density, as well as the topology of the grain boundaries. Predictions of the macroscopic properties of the materials, such as texture, flow stress, fatigue stress, corrosion resistance, magnetization and superconducting critical current, depend heavily on these parameters.

Thanks are due to J. Pflüger and U. Hahn for designing the high-field wiggler and the BW5 beamline at the DORIS III storage ring. The contributions of G. Weichert and R. Giesenberg to the construction of the triple-crystal diffractometer are gratefully acknowledged. The development of efficient software by T. Kracht was crucial for the reliable operation of the diffractometer. Special thanks are due to R. Nowak and A. Swiderski for building the hardware electronics, improving the mechanics and making the diffractometer a user-friendly instrument.

References

Allen, D. A., Howe, R. A., Wood, N. D. & Howells, W. S. (1991) *J. Chem. Phys.* **94**, 5071–5076.

Blume, M. & Gibbs, D. (1988). *Phys. Rev. B*, **37**, 1779–1789.

Egelstaff, P. A. (1983). *Adv. Chem. Phys.* **53**, 1–60.

Eichhorn, K. (1993). *DIF4 User's Guide*. HASYLAB, DESY, Hamburg, Germany.

Frello, T., Poulsen, H. F., Bentzon, M. D., Garbe, S., von Zimmermann, M., Abrahamsen, A. & Andersen, N. H. (1997). Unpublished.

Garbe, S., Poulsen, H. F. & Juul Jensen, D. (1996). *Proc. ICOTOM 11; 11th Int. Conf. Text. Mater.*, Xian, People's Republic of China.

Gibaud, A., Harlow, D., Hastings, J. B., Hill, J. P. & Chapman, D. (1997). *J. Appl. Cryst.* **30**, 16–20.

Hahn, U. (1993). *HASYLAB Annual Report*, pp. 143–145. HASYLAB, DESY, Hamburg, Germany.

Hahn, U., Schulte-Schrepping, H., Balewski, K., Schneider, J. R., Ilinski, P., Lai, B., Yun, W., Legnini, D. & Gluskin, E. (1997). *J. Synchrotron Rad.* **4**, 1–5.

Hastings, J. B., Siddons, D. P., Schneider, J. R. & Berman, L. E. (1989). *Rev. Sci. Instrum.* **60**, 2398–2401.

Kirfel, A. & Eichhorn, K. (1990). *Acta Cryst.* A**46**, 271–284.

Kracht, T. (1994). *SPECTRA*. Technical Note 94–01. HASYLAB, DESY, Hamburg, Germany.

Kracht, T. & Poulsen, H. F. (1995). *BW5 Software Manual*. HASYLAB, DESY, Hamburg, Germany.

Larson, B. C. & Schmatz, W. (1980). *Phys. Status Solidi B*, **99**, 267–275.

Lippert, M., Brückel, T., Köhler, T. & Schneider, J. R. (1994). *Europhys. Lett.* **27**, 537–541.

Lippmann, T. & Schneider, J. R. (1996). *HASYLAB Annual Report*, pp. 996–997. HASYLAB, DESY, Hamburg, Germany.

Messoloras, S., Schneider, J. R., Stewart, R. J. & Zulehner, W. (1989). *Semicond. Sci. Technol.* **4**, 340–344.

Neuefeind, J., Lemke, A. & Bertagnolli, H. (1998). *J. Non-Cryst. Solids*. In the press.

Neuefeind, J. & Liss, K.-D. (1996). *Ber. Bunsenges. Phys. Chem.* **100**, 1341–1349.

Neuefeind, J. & Poulsen, H. F. (1995). *Phys. Scr.* **57**, 112–116.

Neuefeind, J., Zeidler, M. D. & Poulsen, H. F. (1996). *Mol. Phys.* **87**, 189–201.

Neumann, H.-B., Poulsen, H. F., Rütt, U., Schneider, J. R. & von Zimmermann, M. (1995). *Phase Transit.* **55**, 17–35.

Neumann, H.-B., Rütt, U., Bouchard, R. & Schneider, J. R. (1994). *J. Appl. Cryst.* **27**, 1030–1038.

Neumann, H.-B., Rütt, U., Schneider, J. R. & Shirane, G. (1995). *Phys. Rev. B*, **52**, 3981–3984.

Neumann, H.-B., Schneider, J. R., Süssenbach, J., Stock, S. R. & Rek, Z. U. (1996). *Nucl. Instrum. Methods*, A**372**, 551–555.

Pflüger, J. (1992). *Rev. Sci. Instrum.* **63**, 295–300.

Pflüger, J. (1993). *HASYLAB Annual Report*, pp. 140–143. HASYLAB, DESY, Hamburg, Germany.

Pflüger, J. (1994). *HASYLAB Annual Report*, pp. 93–95. HASYLAB, DESY, Hamburg, Germany.

Poulsen, H. F., Frello, T., Andersen, N. H., Bentzon, M. D. & von Zimmermann, M. (1998). *Physica C*. In the press.

Poulsen, H. F., Garbe, S., Lorentzen, T., Juul Jensen, D., Poulsen, F. W., Andersen, N. H., Frello, T., Feidenhans'l, R. & Graafsma, H. (1997). *J. Synchrotron Rad.* **4**, 147–154.

Poulsen, H. F. & Neuefeind, J. (1995). *Nucl. Instrum. Methods Phys. Res. B*, **95**, 509–514.

Poulsen, H. F., Neuefeind, J., Neumann, H.-B., Schneider, J. R. & Zeidler, M. D. (1995). *J. Non-Cryst. Solids*, **188**, 63–74.

Poulsen, H. F., von Zimmermann, M., Schneider, J. R., Andersen, N. H., Schleger, P., Madsen, J., Hadfield, R., Casalta, H., Liang, R., Dosanjh, P. & Hardy, W. (1996). *Phys. Rev. B*, **53**, 15335–15344.

Root, J. H., Egelstaff, P. A. & Hime, A. (1986). *Chem. Phys.* **109**, 437–453.

Rütt, U. (1996). Dissertation, University of Hamburg, Germany.

Rütt, U., Diederichs, A., Schneider, J. R. & Shirane, G. (1997). *Europhys. Lett.* **39**, 395–400.

Rütt, U., Neumann, H.-B., Poulsen, H. F. & Schneider, J. R. (1995). *J. Appl. Cryst.* **28**, 729–737.

Schleger, P., Casalta, H., Hadfield, R., Poulsen, H. F., von Zimmermann, M., Andersen, N. H., Schneider, J. R., Liang, R., Dosanjh, P. & Hardy, W. N. (1995). *Physica C*, **241**, 103–112.

Schleger, P., Hadfield, R., Casalta, H., Andersen, N. H., Poulsen, H. F., von Zimmermann, M., Schneider, J. R., Liang, R., Dosanjh, P. & Hardy, W. N. (1995). *Phys. Rev. Lett.* **74**, 1446–1449.

Schmidt, T. (1992). Diploma thesis, University of Hamburg, Germany.

Schmidt, T. (1995). Dissertation, University of Hamburg, Germany.

Schneider, J. R., Gonçalves, O. D., Rollason, A. J., Bonse, U., Lauer, J. & Zulehner, W. (1988). *Nucl. Instrum. Methods*, B**29**, 661–674.

Schneider, J. R., Nagasawa, H., Berman, L. E., Hastings, J. B., Siddons, D. P. & Zulehner, W. (1989). *Nucl. Instrum. Methods*, A**276**, 636–642.

Shirane, G., Cowley, R. A., Matsuda, M. & Shapiro, S. M. (1993). *Phys. Rev. B*, **48**, 15595–15602.

Strempfer, J. (1997). Private communication.

Strempfer, J., Brückel, T., Rütt, U., Schneider, J. R., Liss, K.-D. & Tschentscher, T. (1996). *Acta Cryst.* A**52**, 438–449.

Vigliante, A., von Zimmermann, M., Schneider, J. R., Frello, T., Andersen, N. H., Madsen, J., Buttrey, D. J., Gibbs, D. & Tranquada, J. M. (1997). *Phys. Rev. B*, **56**, 8248–8251.

Zachariasen, W. H. (1945). *Theory of X-ray Diffraction in Crystals*. New York: Wiley.